Numerical Marfe Studies at ASDEX Upgrade

H. Kastelewicz, R. Schneider, J. Neuhauser, D. Reiter,
B. Braams, K. Büchl, U. Wenzel

IPP 8/3 April 1994

MAX-PLANCK-INSTITUT FÜR PLASMAPHYSIK

85748 GARCHING BEI MÜNCHEN

MAX-PLANCK-INSTITUT FÜR PLASMAPHYSIK

GARCHING BEI MÜNCHEN

Numerical Marfe Studies at ASDEX Upgrade

H. Kastelewicz, R. Schneider, J. Neuhauser, D. Reiter,
B. Braams, K. Büchl, U. Wenzel

IPP 8/3

April 1994

Die nachstehende Arbeit wurde im Rahmen des Vertrages zwischen dem Max-Planck-Institut für Plasmaphysik und der Europäischen Atomgemeinschaft über die Zusammenarbeit auf dem Gebiete der Plasmaphysik durchgeführt.

Numerical Marfe Studies at ASDEX Upgrade

H. Kastelewicz[1], R. Schneider[2], J. Neuhauser[2], D. Reiter[3],
B. Braams[4], K. Büchl[2], U. Wenzel[1]

[1]Max-Planck-Institut für Plasmaphysik, EURATOM Association, Bereich Berlin, D-10117 Berlin, FRG ; [2]Max-Planck-Institut für Plasmaphysik, EURATOM Association, D-85748 Garching/München, FRG ; [3]Forschungszentrum Jülich (KFA), Institut für Plasmaphysik EURATOM Association, D-52425 Jülich, FRG ; [4]Courant Institute, New York University, New York, USA

Abstract

Marfes - as precursors of the density limit in high density discharges - may serve as reliable criteria for discharge controlling in order to avoid disruption. Calculations were made with the B2-EIRENE code package to study the formation and temporal development of marfes and get information about the discharge parameter domain in which marfes exist. The stand-alone version of the B2 code was used to determine the density limit for marfe onset as a function of the input power, the safety factor and the impurity concentration. Good qualitative agreement with available experimental data was obtained. Time-dependent calculations with the full coupled multi-fluid code (deuterium, helium, carbon) show highly dynamic behaviour of marfes. "Steady-state" marfes can be sustained in a dynamic way by appropriately controlling the plasma density or impurity concentration. The impurity radiation pattern of marfes is usually dominated by C^{3+} line radiation, which, therefore, should be suitable for optical monitoring.

1. Introduction

Marfes (or radiation instabilities) are observed as precursors of the density limit in tokamak discharges. They are poloidally localized, axisymmetric structures in the tokamak edge region with strongly enhanced plasma density, reduced temperature and high radiative energy losses due to impurities. Their appearance is accompanied by a strong decrease of the power flux to the divertor plates or even by complete plasma detachment. Marfes are observed as quasi-steady-state configurations or moving phenomena.

The basic mechanism driving the formation of marfes and similar phenomena in quite different fields of research, e.g. astronomical objects / 1 /, is due to a peculiarity of many radiating thermodynamic systems: If the derivation of the radiation function L(T) of a thermodynamic system becomes negative for some range of the temperature T, a thermal instability can develop and result in a region of higher density and lower temperature than the surrounding medium. For tokamak discharges this condition can be provided by different impurities, e.g. carbon ions, where the radiation function may have a maximum at typical boundary plasma temperatures. The general criterion for this instability has been discussed in various papers / 1 - 5 /.
Besides this basic understanding of marfe formation, however, the actual behaviour of marfes and their dependence on the plasma parameters under the complex conditions of tokamak discharges can only be realistically described by appropriate numerical models.

Marfes and their relation to the global density limit have been extensively studied in ASDEX / 6 - 9 /. In order to confirm the validity of the basic marfe model, numerical simulations of the marfe dynamics in realistic ASDEX double-null geometry have been done with the stand-alone version of the B2 code / 9 / as well as with the coupled B2-EIRENE package / 9, 10 /. Because of up-down symmetry and toroidal curvature, a marfe always formes at the high-field-side midplane above a critical edge density. With an experimentally determined carbon density of $0.5\text{-}1\times10^{18}\mathrm{m}^{-3}$, the critical density for marfe onset agrees roughly with the experimental marfe limit for typical ASDEX discharge densities in the range of 1 to 2 $\times$ $10^{19}\mathrm{m}^{-3}$. The anomalous transport coefficients in these runs were adjusted in such a way that experimental edge and divertor quantities below the marfe limit were reasonably fitted / 11 /.

Recent experimental investigations of high-density single-null discharges in ASDEX Upgrade / 12, 13 / show that marfes form preferentially near the (lower) x-point, since the

geometry and the source and sink distributions are completely different. Approaching the density limit, the marfe moves deeper into the main plasma beyond the separatrix; eventually it quickly moves upwards at the high-field side. This marfe evolution is accompanied by a rather complicated pattern of the impurity (mostly carbon ?) radiation. Just as previously observed on ASDEX / 6, 7 /, the critical density for marfe onset was found to depend linearly on the power flowing into the scrape-off layer (SOL) and agrees with theoretical predictions / 2 /.

This paper presents a numerical study of the formation and behaviour of marfes based on a multifluid hydrodynamic description (D-He-C plasma) where the actual geometry and relevant discharge parameter ranges of ASDEX Upgrade single-null discharges are considered. Essential experimental facts will be verified, but, because of basically uncertain assumptions entering the hydrodynamic model (in particular concerning the radial transport laws, the boundary conditions and some other terms entering the basic equations / 14, 11 /), no quantitative simulations of individual discharges have been tried up to now. In some respect, the calculations may therefore be considered as an independent numerical experiment for qualitatively simulating the behaviour of marfes in ASDEX Upgrade discharges. First results have been published in / 15 /.

In sect. 2 we briefly review our numerical model, which is based on the B2 multi-fluid plasma code in conjunction with the EIRENE Monte Carlo code for the neutrals, and give some details about the underlying assumptions.

By means of a simplified version, viz., a single-fluid description and a simplified recycling and radiation model, the temporal formation of a marfe is considered in sect. 3. It is found that, for sufficiently high impurity concentration, marfe formation may be initiated by enhancing the plasma density above a sharply defined critical value. The characteristic time for the evolution of the marfe is of the order of 10ms. In this approximation, contrary to the multi-fluid situation considered in sect. 5, a steady state is reached if the density is kept constant after marfe onset.

In sect. 4 the density limits for the onset and disappearance of marfes are investigated as a function of the input power P and safety factor q. Both limits differ in general, i.e. there exists a hysteresis, which, however, vanishes for low input power and small safety factor. The density limit for marfe onset increases linearly with P, but it is nearly independent of q. Once a marfe is formed, its growth rate due to further rising of the density is found to

increase with the safety factor. Thus, marfes produced at higher q are more pronounced and, hence, are easier to detect experimentally than marfes at lower q.

In sects. 5 and 6 the dynamic behaviour of marfes and their radiation properties are studied on the basis of the full multi-fluid description of a deuterium-helium-carbon plasma.
First, some scenarios of time-dependent calculations are presented in sect. 5. The detailed inclusion of all different ion species and their individual transport and radiation characteristics has the consequence that marfes, once formed, may be highly dynamic, particularly at high density and energy input. Actually, no steady state is found, even if all the boundary conditions are kept constant. By introducing feedback control of the deuterium density or impurity concentration, however, a quasi-steady marfe which allowing rather detailed comparisons with experimental observations can be sustained.

The impurity radiation pattern of the marfe may qualitatively change for the different ion species in the course of a density ramp. It is clearly dominated by the C^{3+} line radiation; the C^{2+} and C^{1+} ions contribute to a lesser extent. The C^{4+} and C^{5+} ions radiate predominantly deeper in the bulk plasma. Helium radiates most extensively at the high-temperature slope of the marfe. A total of about 1/3 to 2/3 of the input energy is lost by radiation in the situations considered.

2. Numerical Model

The edge and divertor plasma is described in the hydrodynamic approximation by the B2 2d multi-fluid code (for the 9 ions of D, He, C), which is self-consistently coupled to the EIRENE 3d Monte-Carlo-code for the neutrals. EIRENE takes into account all essential details of the neutral kinetics and the geometry of the discharge vessel. The principal aspects of the code package have been discussed elsewhere / 10 /. The numerical grid for the B2 code (Fig. 1) is produced from an ASDEX Upgrade equilibrium using the Sonnet grid generator developed at Garching.

Besides this most exact description of the boundary and divertor plasma, which is very computer time consuming, one may also use simplified versions of this code for problems where this seems appropriate.
If, for example, one is not primarily interested in the radiation properties of the plasma, one may use a single-fluid description and include the energy losses by impurity radiation via an ad hoc ansatz in the hydrodynamic energy balance equation. A simple way to simulate the radiation

losses is to consider a fictitious impurity species where the density is assumed to be proportional to the electron density and where the radiation characteristic is roughly that obtained with a finite impurity residence time in the scrape-off layer / 2 /. Thus, we assumed the ansatz

$$P_{rad} \propto n_e^2 / \left[(T_e/15eV)^{1.5} + (T_e/15eV)^{-3} \right]$$

typical of carbon or a mixture of low-z impurities.

Furthermore, if the details of the neutral kinetics is not the main object of interest, one may replace the bulky EIRENE code by a simplified recycling model (calibrated against the full model) to describe the particle source terms of the B2 code. Such models are available in the literature / 16 /. Here we will use a somewhat different model, the basic idea of which is as follows: The motion of the neutrals emitted from the target plates is split into a longitudinal motion parallel to the flux surfaces, where the neutrals are absorbed, i.e. ionized in the usual way, and a radial relaxation process, where the radial profile of this longitudinal particle flux simultaneously relaxes to a prescribed radial flux profile. This radial profile, on the other hand, is calculated as if the neutrals penetrate the plasma radially from the wall side and from the bulk plasma side (according to a given albedo).

Thus, there are three code versions of the hydrodynamic description, which have all been tested to yield marfes for approximately the same parameter regions:

B2(D,He,C) — EIRENE,
B2(D,He,C) — simplified recycling model (deuterium),
B2(D) — simplified recycling and radiation model.

The last version was used here for the extensive scans aimed at finding the parameter domain in which marfes exist. It must be mentioned, however, that particularly the single-fluid approximation turns out to be uncertain when considering the time behaviour of marfes (see sects. 3 and 5).

For the - a priori unknown - anomalous cross-field transport we assume a 1/n transport law using coefficients obtained from a first fit at ASDEX:

Diffusion coefficients: $D = D_0 \cdot \left(3 \cdot 10^{19} m^{-3}/n_i\right), \quad D_0 = 0.5 m^2 s^{-1},$

Thermal conductivity: $\kappa_{e,i} = n_{e,i} \chi_{e,i}, \quad \chi_e = 3 \cdot D, \quad \chi_i = 2 \cdot D.$

Other transport laws may be used in the future when more detailed data are available.

At the physically different boundaries of the numerical grid shown in Fig. 1 appropriate conditions must be prescribed for the density n (or the normal component of the ion flux density, F_n) of each ion species, for the electron temperature T_e and the common ion temperature T_i (or the corresponding normal components of energy fluxes $F_{e,e}$, $F_{e,i}$) and for the parallel velocity of each ion species, u_p. For the present calculations this was done in the following way:

At the bulk plasma side we assume the densities of the lower-charged ions to vanish, i.e. $n_{He^{1+}} = n_{C^{1+}} = n_{C^{2+}} = n_{C^{3+}} = 0$, and choose $n_{D^{1+}}$, $n_{He^{2+}}$ and $n_{C^{4+}} = n_{C^{5+}} = n_{C^{6+}}$ so as to get the desired plasma density and impurity concentration. At the wall near boundary of the grid we set explicitly only the density of C^{1+} in order to simulate carbon influx from the wall. The other densities are allowed to be adjusted by the code since we only impose conditions on the ion flux densities through $F_n = -\alpha n$ ($\alpha = 100$m/s). This relation is suggested from the generally observed exponential density decay:

$F_n \propto D\frac{\partial n}{\partial y} \propto \frac{D}{\lambda_n} n$, $\frac{D}{\lambda_n} = 100\frac{m}{s}$ for $D = 1m^2/s$ and $\lambda_n = 1$cm.

The same boundary condition is assumed for all ion fluxes at the private region side. At the target plates, the ansatz $\frac{\partial n}{\partial x} = 0$ was used for simplicity. The particular form of this condition was found to influence the plasma solution only in the immediate neighbourhood of the plates.

To describe the boundary conditions for the energy equations at the bulk plasma side, one may use either the electron and ion energy fluxes or the temperatures T_e and T_i, which is physically equivalent as far as steady states are concerned. Usually we prefer the energy fluxes since they are more obviously connected with the corresponding discharge parameters (where we roughly assume $F_{e,i} \approx F_{e,e}$). For highly dynamic states, of course, both cases would imply different assumptions on the actual response of the main plasma.
At the wall and at the private region side we always put $T_e = T_i = 2$eV, while at the plates the usual ansatz for the convective energy fluxes is made (see below).

Finally, the boundary conditions for the parallel velocity are fixed in the following way: At the bulk plasma boundary we set $u_p = 0$, and near the wall vanishing shear is assumed, $\frac{\partial u_p}{\partial y} = 0$. A modified version of the latter condition ('limited shear') is also adopted at the private region side. At the targets $M^* = 1$ is used for each species, where M^* is the isothermal Mach number calculated from the total plasma pressure.

The whole set of boundary conditions can be summarized as follows (the ion species index is omitted):

Bulk plasma side

n , (F_n) and

$u_p = 0$ for each ion species of D, He, C

$\mathbf{F_{e,e}}$, $\mathbf{F_{e,i}}$ or $\mathbf{T_e}$, $\mathbf{T_i}$ for electrons and ions

Private region

$F_n = -\alpha n$ and

$\frac{\partial}{\partial y}\left(\frac{u_p}{\sqrt{T_i}}\right) = 0$ for each ion species

$T_e = T_i$ = 2eV for electrons and ions

Wall side

n , (F_n) for C^{1+} and $F_n = -\alpha n$ for the other ion species

$\frac{\partial u_p}{\partial y} = 0$ for each ion species

$T_e = T_i$ = 2eV for electrons and ions

Target plates

$\frac{\partial n}{\partial x} = 0$ and

$u_p = c_s M^*$, $M^* = 1$ for each ion species

(c_s = sound velocity)

$F_{e,e} = -\beta_e u n_e T_e$, $\beta_e = 4.0$ for electrons

$F_{e,i} = -un\frac{m}{2}u_p^2 - \beta_i u n T_i$, $\beta_i = 2.5$

for ions ($u = c_s B_\Theta / B$)

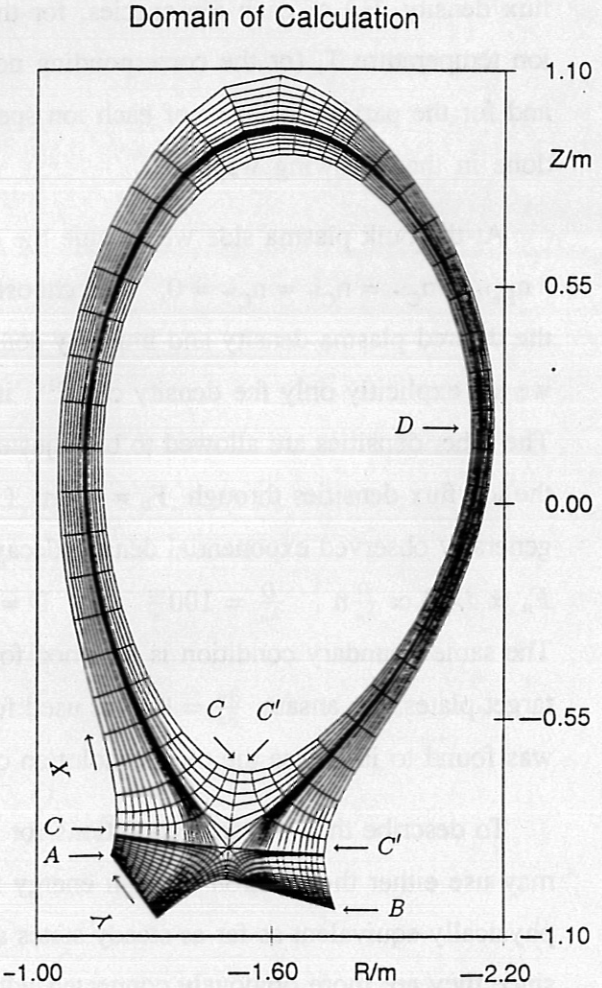

Fig. 1
Calculational grid for the B2 code. The letters *A*, *B* denote the inner and outer target plate, respectively. *C*, *C*' and *D* mark poloidal positions (near the x-point and outer midplane) referred to later in the text. *X* is the poloidal and *Y* the radial coordinate, where *Y* = 0 at the bulk plasma and private region boundary.

The bold-faced variables above are the essential input parameters: the ion densities and energy fluxes (or temperatures) at the bulk plasma side and the ion densities at the wall side of the grid.

The surface integral of the energy flux densities is the input power P into the calculational region. Compared with experiment, $P = P_{tot} - P_{rad}$, where P_{tot} and P_{rad} are the total energy input and the energy radiated by the inner bulk plasma, respectively. P is the reference power used in this paper.

Since no detailed information is available from experiments about the poloidal dependence of all these quantities at the inner boundary, we assume constant values, which should be appropriate if the calculational grid extends deep enough into the main plasma.

We define a reference density for the boundary plasma since the line-averaged density used in experiments is not an appropriate quantity for the present model. To be independent of the particular calculational grid, it would be appropriate to use, for example, the average density at the separatrix. However, when considering marfe plasma states it turns out that the density at the separartix may strongly vary with the particular shape and location of the marfe itself, even if the density deeper in the main plasma (at the inner grid boundary) is practically not changed. Therefore, the reference density used in the following will be the poloidally averaged density at the inner grid boundary, $\overline{n_{e,grd}}$, or the local inner grid boundary density at the outer midplane (position D in Fig. 1), $n_{e,grd}$, both of which are less influenced by the particular marfe configuration.

3. Marfe Formation

The mechanism of marfe formation is based on the particular form taken by the radiation characteristics of impurity ions, which have maximum radiated energy at relatively moderate temperatures, say T_e of the order of 10 –20eV. Thus, starting from a high-temperature state and lowering the plasma temperature, e.g. by enhancing the plasma density, the radiated energy will increase due to the radiation characteristics. At some local position where the radiating volume is particularly large and the temperature gradients are small (above all, this should be the case near the x-point because of the widely spaced flux surfaces), it may happen that the radiated energy exceeds the possible energy influx into this region. Consequently, the local plasma temperature will further decrease, leading again to enhancement of the radiation efficiency. Simultaneously, because of the pressure balance along the field lines, the plasma density will increase in this region of low temperature, which also enhances the radiation losses.

Thus, there are two coupled effects that drive a nonlinear instability ('thermal condensation instability'), which builds up a high-density low-temperature plasma region ('marfe'). In

the tokamak such marfes represent axisymmetric belts in the boundary plasma, mostly near the (lower) x-point.

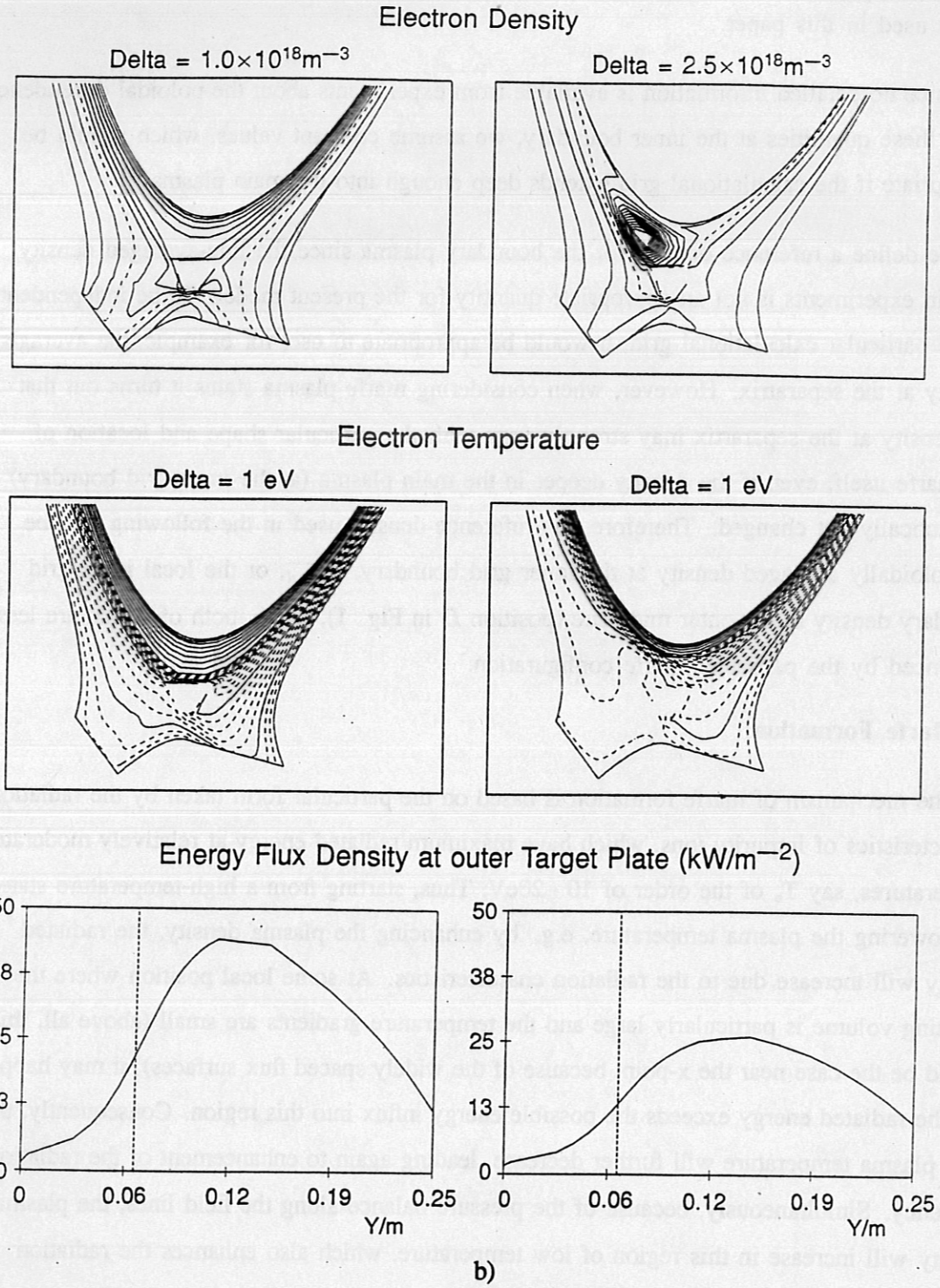

Fig. 2
a) Edge plasma state just before marfe formation ($n_{e,grd} = 0.95 \cdot 10^{19} m^{-3}$)
b) Edge plasma stare just after marfe formation ($n_{e,grd} = 1.00 \cdot 10^{19} m^{-3}$)

Marfe formation is initiated numerically by successively enhancing the plasma density (i.e. the density at the boundary) for sufficiently high impurity concentration (≈5% carbon). Above a sharply defined critical density a marfe is formed, this being accompanied by a reorganization of the whole edge plasma state. As a consequence, strong changes are experimentally observed, e.g. enhancement of the impurity radiation and bremsstrahlung in the vicinity of the marfe, development of a cold and dense divertor and decrease of the total power flux and change of the power deposition profile at the target plates.

Figures 2a,b compare calculated contour plots of the electron density and temperature and the power deposition profiles at the outer target plate just before and just after marfe formation, which confirm these findings. Both plasma states are steady-state solutions of the single-fluid model in conjunction with the simplified recycling and radiation model. The plasma density differs in this case by about 5% ($n_{e,grd} = 0.95 \cdot 10^{19} m^{-3}$ and $n_{e,grd} = 1.00 \cdot 10^{19} m^{-3}$, respectively), all other discharge parameters being the same (P = 1MW, safety factor q = 4.5, impurity concentration c_{imp} = 5%). The location of the marfe is clearly identified by the strongly enhanced density and low temperature inside the separatrix near the x-point (Fig. 2b). The density maximum is $n_{e,max} = 4.55 \cdot 10^{19} m^{-3}$. The shape of the marfe, its location and the changes of plasma parameters caused by the marfe may, however, strongly vary with the discharge parameters.

The abrupt marfe formation becomes obvious from a time dependent calculation starting from a marfe-free plasma state and moderately enhancing the plasma density. Here we use again the simplified single-fluid approach. Figure 3 shows the temporal evolution of the radial profiles of the electron temperature and density at the poloidal position of the marfe centre and along the outer divertor plates if the boundary condition for the plasma density is linearly changed so as to enhance $n_{e,grd} = 0.6 \cdot 10^{19} m^{-3}$ ($\overline{n_{e,grd}} = 0.7 \cdot 10^{19} m^{-3}$) up to $n_{e,grd} = 1.0 \cdot 10^{19} m^{-3}$ ($\overline{n_{e,grd}} = 1.1 \cdot 10^{19} m^{-3}$) within 200 ms. Marfe formation starts after about 170ms. In this approximation the plasma finally attains a steady state (that of Fig. 2b) if the density is kept constant. The actual value of the steady-state density at the marfe centre depends, of course, on the final plasma density and increases with the latter according to the curves shown in Fig. 7.

A steady state is reached in about 25ms. This is comparable to the characteristic time for marfe formation, since practically the same time is needed to build up the marfe if we

start from the pre-marfe state of Fig. 2a with $n_{e,grd} = 0.95 \cdot 10^{19} m^{-3}$ ($\overline{n_{e,grd}} = 1.0 \cdot 10^{19} m^{-3}$) and assume a step-like density increase up to the state of Fig. 2b with $n_{e,g} = 1.0 \cdot 10^{19} m^{-3}$ ($\overline{n_{e,grd}} = 1.1 \cdot 10^{19} m^{-3}$).

Preceeding marfe onset there is a strong temperature decrease at the divertor plates (more pronounced at the inner plate) which extends over the whole divertor when the marfe builds up. The density profile at the plates slightly flattens.

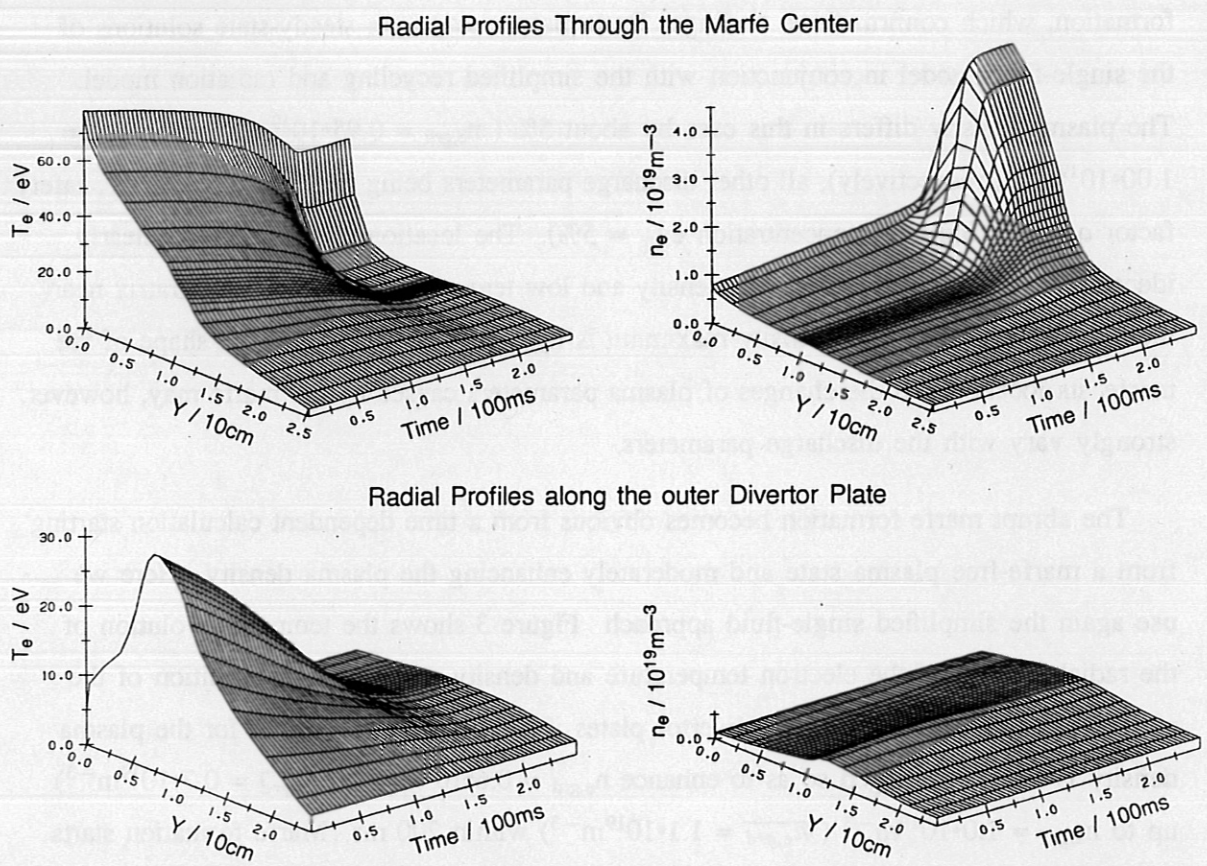

Fig. 3
Temporal evolution of the radial profiles of the electron density and temperature at the poloidal position of the marfe centre and along the outer divertor plate for a linear plasma density rise: $n_{e,grd}(t = 0) = 0.6 \cdot 10^{19} m^{-3} \rightarrow n_{e,grd}(t \geq 200ms) = 1.0 \cdot 10^{19} m^{-3}$.

4. Marfe Limits and Growth Rates

The limits for marfe onset and disappearence were determined as a function of the input power P, safety factor q and plasma density $n_{e,grd}$. Because of computer time restrictions, these calculations were done using the single-fluid description (simplified recycling and radiation model, impurity concentration c_{imp} = 5%) on the assumption that this is a fairly good approximation at the initial stage of marfe formation.

Figures 4 and 5 show the density limit for marfe onset (full lines) and disappearence (broken lines) as function of P (for q = 4.5) and as a function of q (for P = 1MW and P = 3MW), respectively.

As a function of $P = P_{tot} - P_{rad}$ one finds a linear increase of the threshold density for marfe onset, which is also observed experimentally / 6, 7, 13 / for the same range of discharge parameters. Starting from the marfe state and decreasing the plasma density, the marfe can exist down to densities much lower than the threshold density for marfe onset (broken lines in Figs. 4, 5). Thus, there exists a hysteresis which vanishes for small P but which becomes very pronounced for high energy influx. This may be important if one intends to extinguish marfes in the course of experiments by enhancing the input power. (The irregularities of the broken curves are due to the influence of the particular marfe configuration itself on the reference density $n_{e,grd}$ when approaching the lower theshold.)

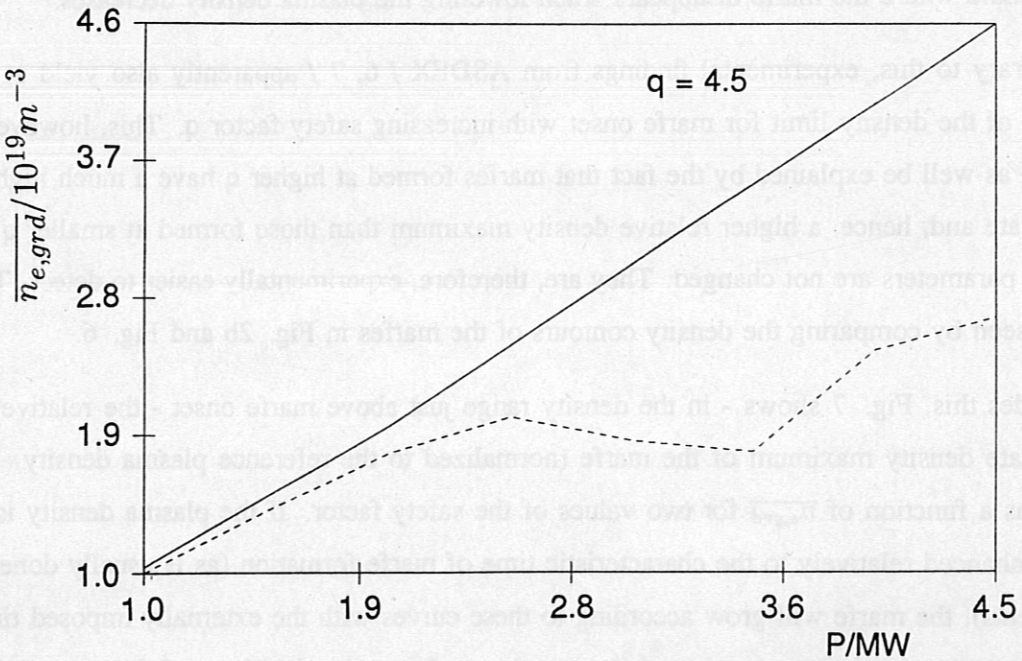

Fig. 4
Density limit for marfe onset (full lines) and for the disappearance of marfes (broken lines) as function of the input power P for q = 4.5

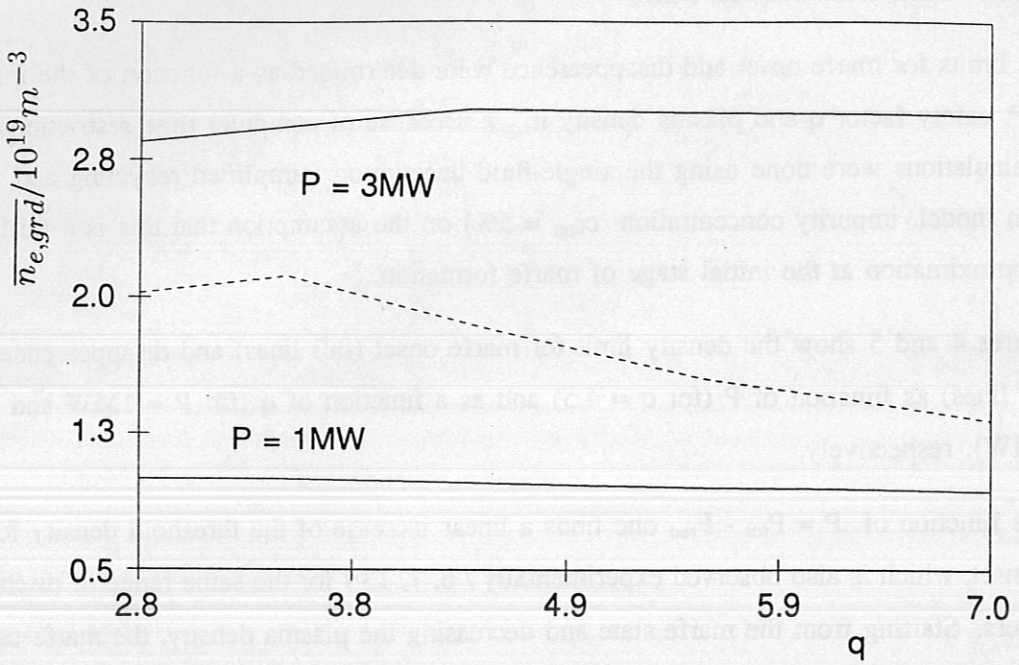

Fig. 5
Density limit for marfe onset (full lines) and for the disappearance of marfes (broken line) as a function of the safety factor q for P = 3MW and P = 1MW

The calculations yield practically no dependence of the density limit for marfe onset on the safety factor q, but the hysteresis (for high enough P) becomes broader with increasing q, i.e. the threshold where the marfe disappears when lowering the plasma density decreases.

Contrary to this, experimental findings from ASDEX / 6, 7 / apparently also yield a decrease of the density limit for marfe onset with increasing safety factor q. This, however, may just as well be explained by the fact that marfes formed at higher q have a much higher growth rate and, hence, a higher relative density maximum than those formed at smaller q if all other parameters are not changed. They are, therefore, experimentally easier to detect. This may be seen by comparing the density contours of the marfes in Fig. 2b and Fig. 6.

Besides this, Fig. 7 shows - in the density range just above marfe onset - the relative steady-state density maximum of the marfe (normalized to the reference plasma density $\overline{n_{e,grd}}$) as a function of $\overline{n_{e,grd}}$ for two values of the safety factor. If the plasma density is slowly enhanced relatively to the characteristic time of marfe formation (as is usually done in experiments), the marfe will grow according to these curves with the externally imposed time scale. Since the density maximum and its growth rate (given by the slope of these curves) are much higher for larger q, in particular immediately after marfe formation, marfes at high q may already be detected (or cause a disruption) at smaller plasma density.

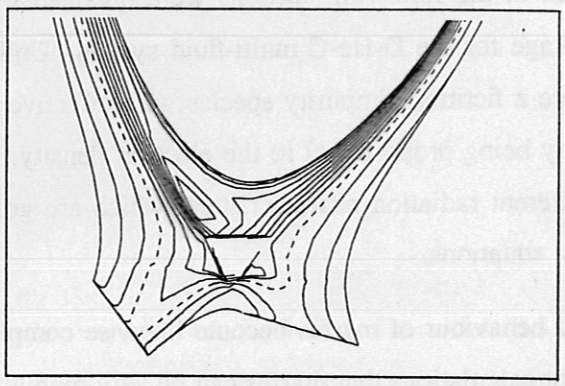

Fig. 6
Marfe for the same conditions as in Fig. 2b but for smaller safety factor q = 2.8; $\overline{n_{e,grd}}$ = $1.1 \cdot 10^{19} m^{-3}$ ($n_{e,grd} = 1.0 \cdot 10^{19} m^{-3}$)

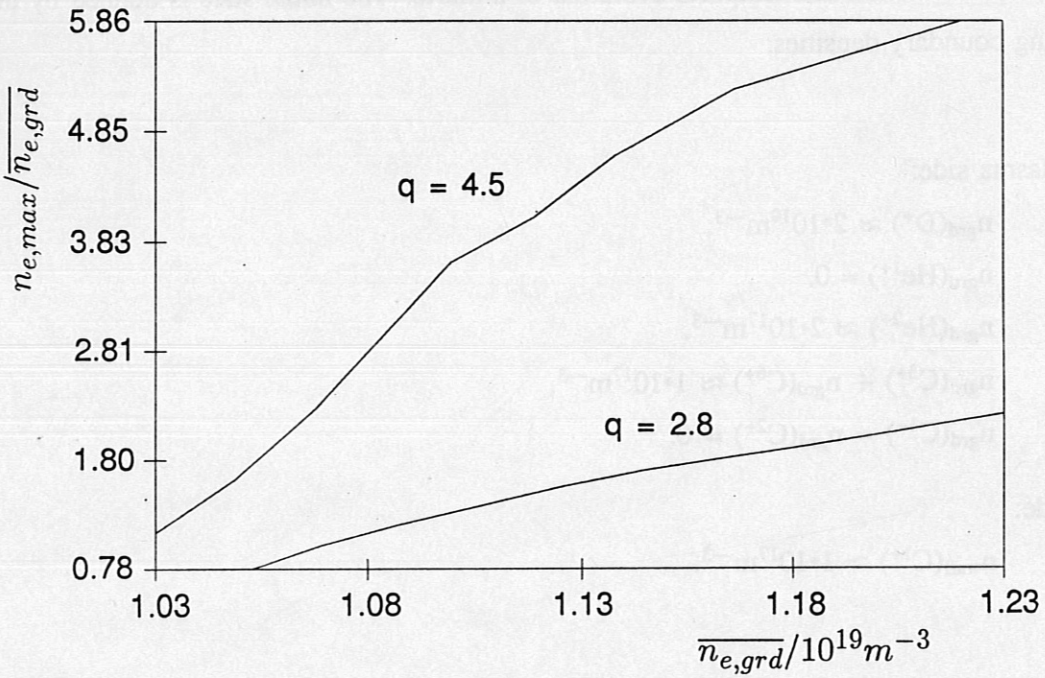

Fig. 7
Normalized marfe density peak as a function of $\overline{n_{e,grd}}$ just above marfe onset for q = 2.8 and for q = 4.5

5. Marfe Dynamics

All results presented in the following sections were obtained with the full coupled B2–EIRENE code package for the D-He-C multi-fluid system. Unlike the situation of the single-fluid model where a fictitious impurity species with effective radiation characteristics was assumed, its density being proportional to the electron density, we now have 8 different impurity ions (with different radiation characteristics) which are governed by individual moment and continuity equations.

The appearance and behaviour of marfes become likewise complicated. In particular, it is found by time-dependent calculations that marfes can be very mobile and that steady states will usually not be reached (in contrast to the single-fluid model) or only for special conditions in the present approximation. In the following, we consider only specific time-dependent scenarios.

First, starting from a marfe-free stationary plasma state and enhancing the plasma density, we trace the formation and temporal evolution of a marfe. The initial state is defined by the following boundary densities:

Bulk plasma side:

$$n_{grd}(D^{+}) \approx 2 \cdot 10^{19} m^{-3},$$
$$n_{grd}(He^{1+}) = 0,$$
$$n_{grd}(He^{2+}) \approx 2 \cdot 10^{17} m^{-3},$$
$$n_{grd}(C^{3+}) \div n_{grd}(C^{6+}) \approx 1 \cdot 10^{17} m^{-3},$$
$$n_{grd}(C^{1+}) = n_{grd}(C^{2+}) = 0.$$

Wall side:

$$n_{wall}(C^{1+}) \approx 1 \cdot 10^{17} m^{-3}.$$

The input power is P = 1MW; it will be kept fixed during the calculations, unless otherwise explicitly stated. The total energy fluxes onto the inner and outer target plates are P_{targ}(inn.) ≈ 150kW and P_{targ}(out.) ≈ 400kW; the energies radiated by the helium and carbon ions are P_{rad}(He) ≈ 30kW and P_{rad}(C) ≈ 70kW, respectively. The remaining relatively high fraction of the input energy flows to the wall, in this case because of the high radial transport coefficients resulting from the 1/n transport law.

The basic scenario of the presumed density control is shown in Fig. 8. In a first step the boundary densities of all ion species were linearly enhanced within 3ms ($0 \leq t \leq 3$ms) up to a factor 2 relative to their initial values and then kept constant. Starting at 37ms, this density rise was continued in alternative ways : (i) within 10ms ($37 \leq t \leq 47$ms) up to a factor 3, and (ii) within 25ms ($37 \leq t \leq 62$ms) up to a factor 2.13 relative to the original values. The latter case (broken line) corresponds to a rather smooth density enhancement which stopped shortly after marfe onset. Finally, the densities are lowered to their previous values in the time interval ($89.3\text{ms} \leq t \leq 99.3$ms).

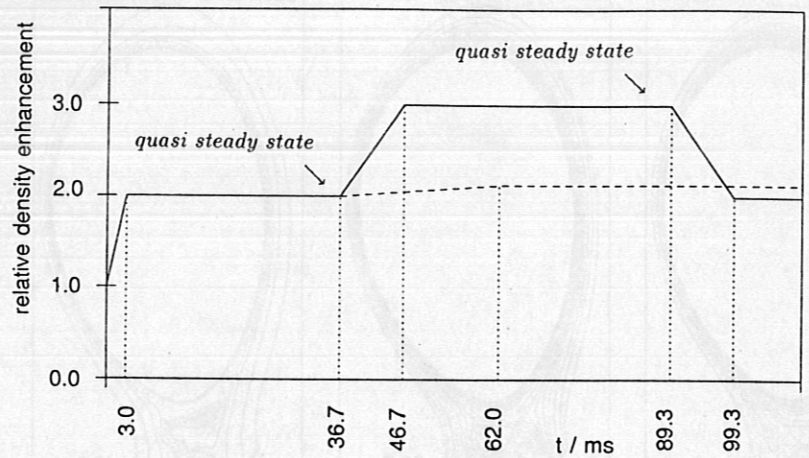

Fig. 8
Presumed time dependency of the boundary densities for multifluid calculations (see text)

The assumed density changes are relatively strong compared with experimental situations, but they are chosen in this way in order to get physical effects with reasonable computer time. The equivalent times in the experiments are usually around a second.

Figures 9 show the electron density contour plots of the initial plasma state and some intermediate states obtained for the steep density ramps in Fig. 8 (full line).

The first density rise puts the plasma in a quasi-steady state at $t \approx 37$ms, which is just below marfe onset ($n_{e,grd} = 3.5 \cdot 10^{19} m^{-3}$). There are clear relative density maxima in both divertors ($n_{e,max} = 3.3 \cdot 10^{19} m^{-3}$) and at the x-point ($n_{e,max} = 4.0 \cdot 10^{19} m^{-3}$), but no locally enhanced impurity radiation in these regions. The total radiated energy, however, is increased to about $P_{rad}(C) = 0.2$MW for carbon and decreased to $P_{rad}(He) = 19$kW for helium. (The latter radiates mostly in the viciniy of the x-point.) At the divertor plates the plasma has been cooled

from about 15eV to 2eV immediately after the beginning of the density ramp (within about 3ms), while the density has been raised more slowly (within ≈20ms) by about a factor of 3.

During the second density ramp the density maxima move from the divertors to the x-point, where the marfe is now rapidly formed. A configuration like that of Fig. 9 for t = 45.3 ms, where the marfe is well localized near the x-point, is experimentally most interesting since it is compatible with stable plasma operation, but it appears here only transiently. It will be considered in more detail below.

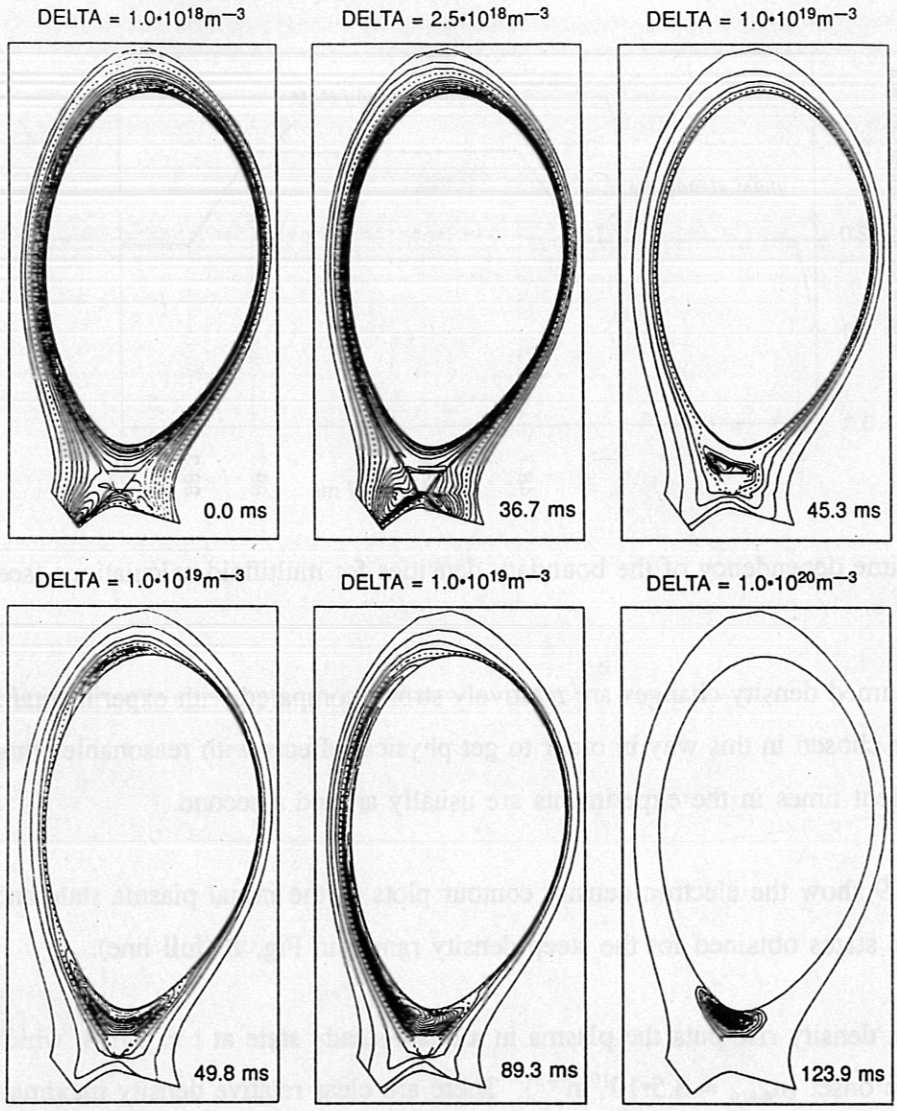

Fig. 9
Electron density contour plots at intermediate plasma states obtained from a time-dependent calculation according to the density ramp in Fig. 8 (full line)

The further development of the marfe depends in a complicated way on how far the densities have been enhanced during the ramp. If we strongly enhance the densities (as shown by the full line in Fig. 8), the energy radiated by the marfe far exceeds heat conduction. The marfe quickly extends towards the hot grid boundary while simultaneously a second marfe is formed at the upper side of the boundary plasma, which links up with the original one at the high-field plasma side. Finally, a quasi-steady state is reached which is characterized by a very extended cold and high-density plasma region ($n_{e,max} = 1.7 \cdot 10^{20} m^{-3}$) at the high field side of the torus (Fig. 9, t = 89.3 ms)). For an even steeper density ramp (relative density enhancement by a factor of 4 instead of 3 in Fig. 8) no x-point marfe is formed at all, but two such cold and dense plasma zones build up at the upper and lower sides directly. Obviously, these plasma states are physically questionable since they are too close to the numerical grid boundary.

When the plasma density is reduced in a third step to its previous value as shown in Fig. 8 , the marfe neither vanishes nor really detaches from the grid boundary but shrinks, while the density maximum further increases (Fig. 9, t = 123.9 ms). A hysteresis is thus observed here, too.

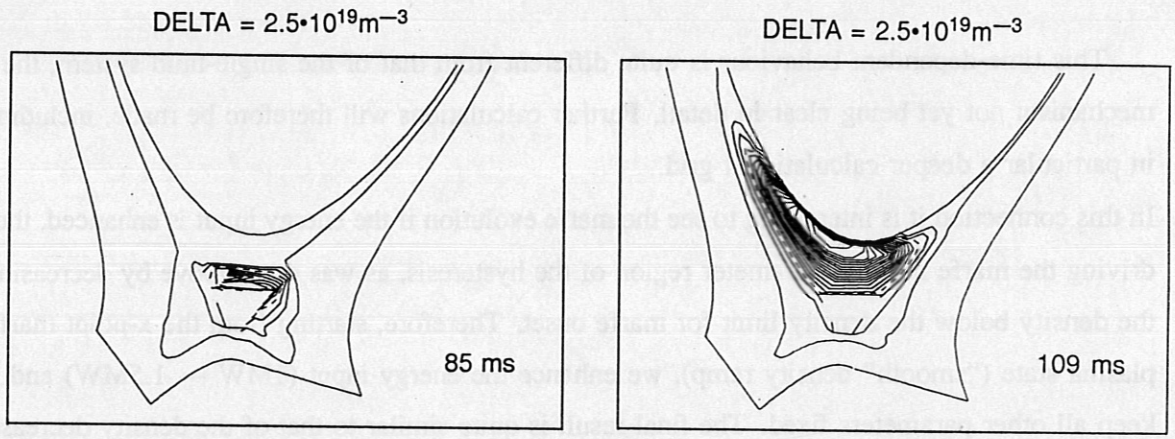

Fig. 10
x-point marfe (t = 85ms) and final marfe stage (t = 109ms) after the "smooth" density ramp in Fig.8 (broken line)

In the alternative case, keeping the density fixed slightly above marfe onset, the marfe growths more slowly and remains poloidally limited to the lower region of the boundary plasma (Fig. 10); no satellite is formed. But also in this case the marfe moves inward up to the grid boundary by virtue of its own dynamics by successively cooling the hot plasma layers in front of it, as can be clearly seen from the time evolution of the radial n_e and T_e profiles in Fig. 11 obtained at the poloidal position *C* (Fig. 1) adjacent to the x-point. Thus, for $t \geq 100$ ms

one again ends up with a marfe close to the grid boundary (Fig.10) which is more compact than the former one in Fig. 9 but has an even higher maximum density ($n_{e,max} = 6 \cdot 10^{19} m^{-3}$). The remaining fluctuations of the density profile in Fig. 11 are partly due to poloidal oscillations of the marfe around its mean position.

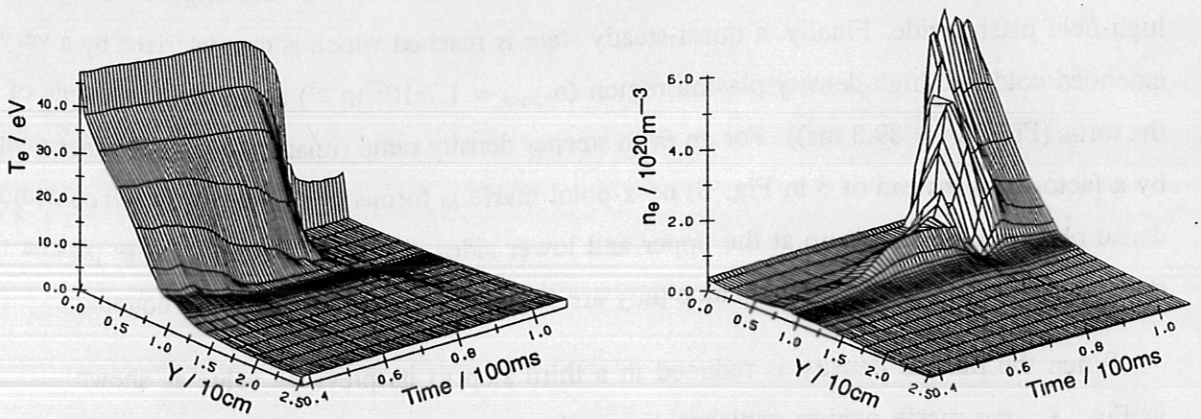

Fig. 11
Temporal evolution of the radial profiles of the electron density and temperature at the poloidal position *C* (Fig.1) obtained for the "smooth" density ramp shown in Fig. 8 (broken line)

This time-dependent behaviour is quite different from that of the single-fluid system, the mechanism not yet being clear in detail. Further calculations will therefore be made, including in particular a deeper calculational grid.
In this connection it is interesting to see the marfe evolution if the energy input is enhanced, thus driving the marfe into the parameter region of the hysteresis, as was done above by decreasing the density below the density limit for marfe onset. Therefore, starting from the x-point marfe plasma state ("smooth" density ramp), we enhance the energy input (1MW → 1.5MW) and keep all other parameters fixed. The final result is quite similar to that of the density decrease shown in Fig. 9 (t = 123.9ms) , i.e. the marfe grows further and moves to the grid boundary.

In contrast to this intrinsically transient behaviour of marfes, experimental findings from ASDEX Upgrade show that marfes can also remain stationary near the x-point inside the separatrix for seconds if the discharge conditions are appropriately controlled / 13 /. One may model this by introducing an internal feedback loop which couples the plasma density or, alternatively, the impurity concentration to the electron temperature at a prescribed point of the boundary plasma (e.g. T_e at the separatrix in the outer midplane, i.e., position *D* in Fig. 1). If the temperature decreases, the plasma density should be reduced and vice versa. In this way, by keeping $T_e(D)$ approximately fixed the marfe can be stabilized near the x-point.

We do this here by starting from the x-point marfe of Fig. 10 (t = 85ms) and multiplying the boundary density by the factor $1/\left[1+(20eV/T_e(D))^2\right]$, thus keeping near $T_e(D) \approx 20$ eV, which corresponds to the actual temperature of the x-point marfe in Fig. 10. The result is shown in Figs. 12, 13 and should be compared with the uncontrolled case of Figs. 10 and 11 where the density has been kept fixed. The temporal plot of the radial density profiles shows that the marfe is permanently kept apart from the grid boundary and prevails near the x-point inside the separatrix. The density contour plot of the controlled marfe at the time t = 98ms looks similar to that of the starting x-point marfe, while in the uncontrolled case the marfe has already became attached to the grid boundary at that time as shown in Fig. 11. Due to the feedback loop the marfe density in Fig. 12 fluctuates around a mean value which is much lower than the final value of the uncontrolled (non-physical) case.

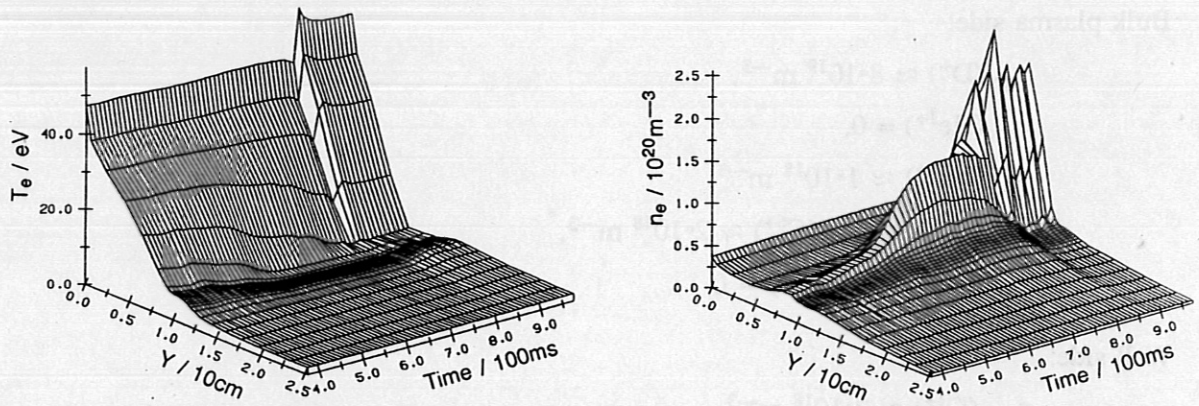

Fig. 12
Temporal evolution of the radial profiles (poloidal position *C* in Fig. 1) of the electron density and temperature just as in Fig. 11 but with controlled plasma density for t ≥ 85ms (see text)

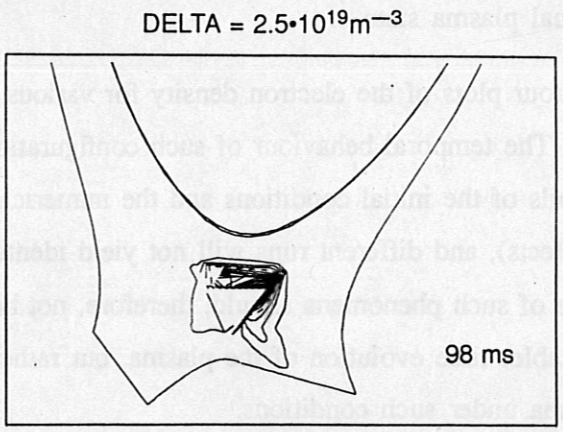

Fig. 13
Electron density contour plot for a controlled x-point marfe (final state of Fig. 12 at t =98ms)

Towards lower temperatures $T_e(D)$ the marfe becomes stronger and moves to the high-field side and closer to the core plasma but remains stable. It is interesting to note that the self-adjusted plasma density (or the impurity concentration, if this quantity is controlled) may oscillate down to values far below the density for marfe onset.

We still want to show that, depending on the chosen boundary conditions, one may get highly dynamic marfe plasma states. Within milliseconds marfes may move in a complicated way around the lower x-point region, into the divertor or upwards along the edge plasma (preferably at the inner, but also at the outer side of the torus), they may change intensity, deform, even split into separate parts and reconnect again. As an example we consider here a case of high density and energy input given by the following boundary conditions, which are kept constant during the calculation:

Bulk plasma side:

$$n_{grd}(D^+) \approx 8 \cdot 10^{19}\ m^{-3},$$
$$n_{grd}(He^{1+}) = 0,$$
$$n_{grd}(He^{2+}) \approx 1 \cdot 10^{18}\ m^{-3},$$
$$n_{grd}(C^{3+}) \div n_{e,grd}(C^{6+}) \approx 2 \cdot 10^{18}\ m^{-3},$$
$$n_{grd}(C^{1+}) = n_{grd}(C^{2+}) = 0.$$

Wall side:

$$n_{wall}(C^{1+}) \approx 2 \cdot 10^{18}\ m^{-3}.$$

Instead of the input power P the temperatures at the bulk plasma side are prescribed, $T_{e,grd} = T_{i,grd} = 100eV$, which results in an input power in the range $5MW \leq P \leq 9\ MW$, depending on the actual plasma state.

Fig. 14 show contour plots of the electron density for various successive times (t = 0 is chosen arbitrarily). The temporal behaviour of such configurations depends sensitively, of course, on the details of the initial conditions and the numerical procedure (e.g. time steps, Monte Carlo effects), and different runs will not yield identical solutions for longer times. The occurrence of such phenomena should, therefore, not be taken as a definite (and experimentally observable) time evolution of the plasma, but rather may reflect a chaotic behaviour of the plasma under such conditions.

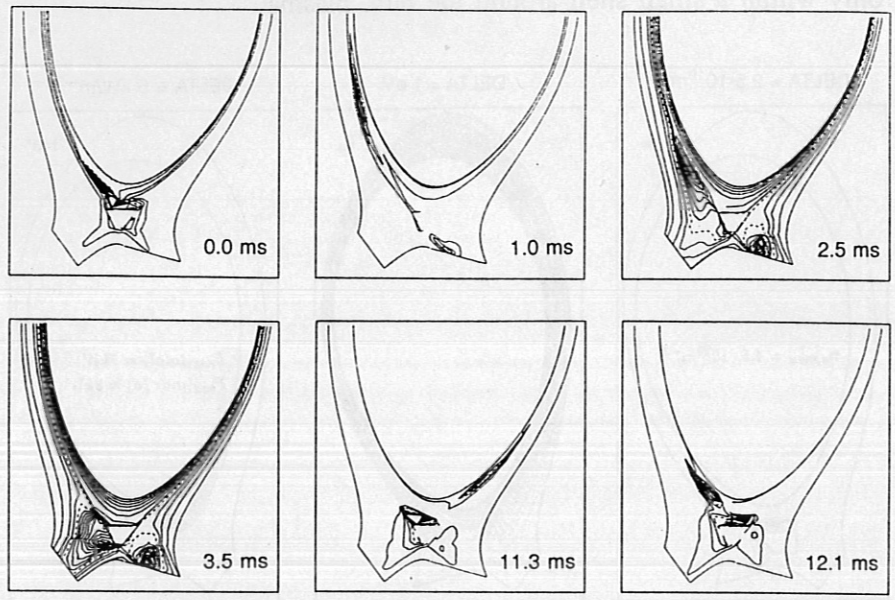

Fig. 14
Temporal marfe evolution at high density and energy input

5. Radiation and Plasma Profiles

The pattern of impurity radiation emitted by the marfe depends sensitively on the shape and intensity of the marfe. As a quite general result for the D-He-C plasma we find that, for the fully developed marfe, mainly the C^{3+} and to a lesser extent C^{2+} , C^{1+} and He^{+} ions contribute to the radiation losses of the marfe. C^{4+} and C^{5+} radiate almost homogeneously within a small shell at the inner grid boundary.

We consider a quasi-steady (controlled) x-point marfe which is of the greatest practical interest since it is compatible with stable discharge operation. Figures 15 show the contour plots of the electron density, electron temperature and line radiation intensities of the different ion species for the marfe of Fig. 13 ($T_e(D) \approx 20$eV). This plasma state is characterized by a density peak near the x-point and a cold divertor with temperatures of about 1eV. The helium line radiation is very small in this case ($P_{rad} \approx 7$kW) but has a clear maximum well separated from the density maximum at the high-temperature slope of the marfe due to the relatively high excitation level of He^{+} of about 20eV. In the mean, C^{1+} radiates mainly in the outer plasma layer, as is to be expected from the proposed boundary condition, while C^{2+} — C^{3+} radiate successively more inward. This can be quantitatively seen from the radial radiation

profiles at the outer midplane (position D in Fig. 1) shown in Fig. 16. C^{4+} and C^{5+} radiate practically only within a small shell around the bulk plasma.

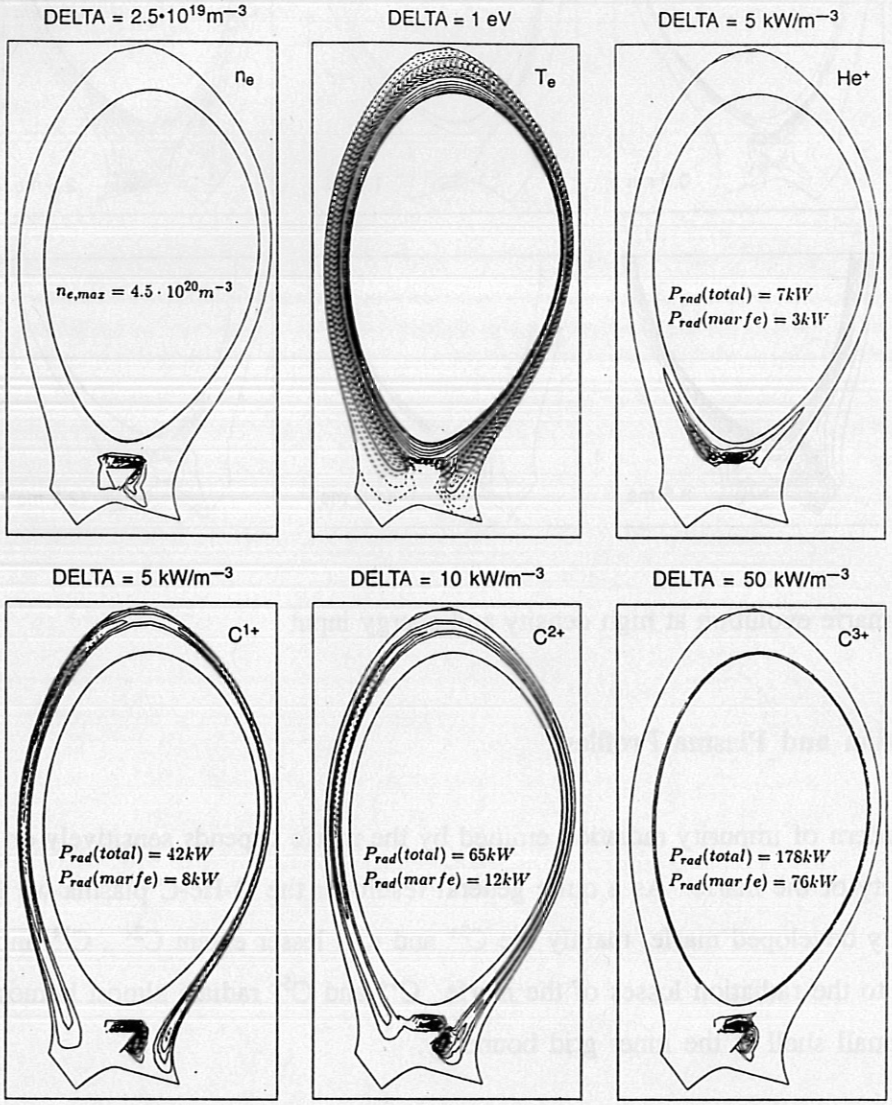

Fig. 15
Contour plots of the electron density and temperature and of the line radiation for helium and carbon ions for the controlled x-point marfe of Fig. 13

The marfe is most clearly seen against the background in the light of the C^{3+} ions, with less intensity also in the C^{2+} and C^{1+} light due to the enhanced intensity in this plasma region. It should be noted that the C^{2+} and C^{1+} radiation have a second maximum apart from the marfe centre more to the outside which also coincides with experimental observations / 13 /. If the marfe becomes stronger (by lowering the controlling separatrix temperature, say to $T_e(D) \approx 15$ eV) this second maximum becomes less pronounced than the first one.

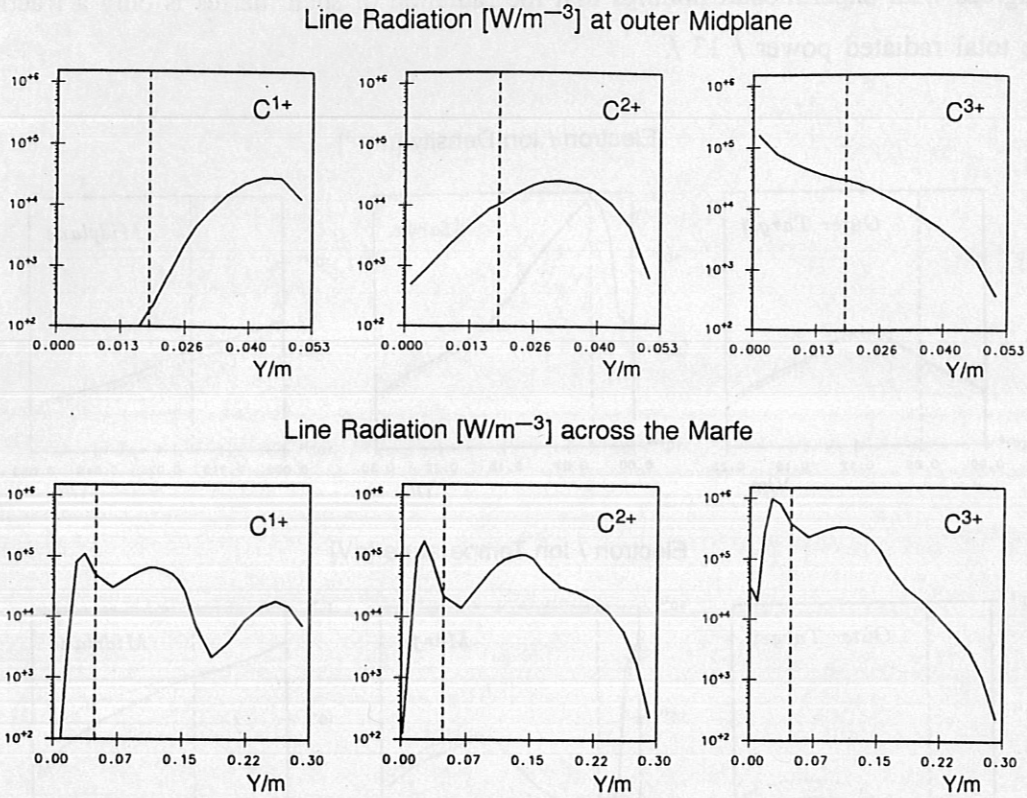

Fig. 16
Radial line radiation profiles of carbon ions at the outer midplane and through the centre of the marfe (poloidal positions *D* and *C'* in Fig. 1) for the controlled x-point marfe plasma state of Fig. 13. The vertical broken line marks the position of the separatrix. Y = 0 at the bulk plasma grid boundary.

The quantitative relations between the radiation intensities of the different carbon ions due the marfe near the x-point and the mean background radiation become obvious from the radiation profiles through the marfe centre and along the outer midplane in Fig. 16. The maximum intensity of C^{3+} is about 1MW/m^3 and exceeds the radiation of the surrounding plasma by more than an order of magnitude. The two maxima of C^{2+} are nearly of equal height but a factor of 5 lower than that of C^{3+}. As may be seen by comparison with the density and temperature profiles in Fig. 17, the carbon radiation maximum coincides with the density maximum and the temperature minimum of the marfe. This has in effect also been found for the highly dynamic marfes of Fig. 14. The details, however, depend sensitively on the particular marfe configuration.

The total power radiated by the impurity ions in the boundary plasma (calculational domain) is for the x-point marfe P_{rad}(total) $\approx$ 300kW (about 30% of the input power). The power radiated by the marfe itself, on the other hand, is only P_{rad}(marfe) $\approx$ 100kW.

This agrees with experimental findings that the radiation of such marfes is only a fraction of the total radiated power / 13 /.

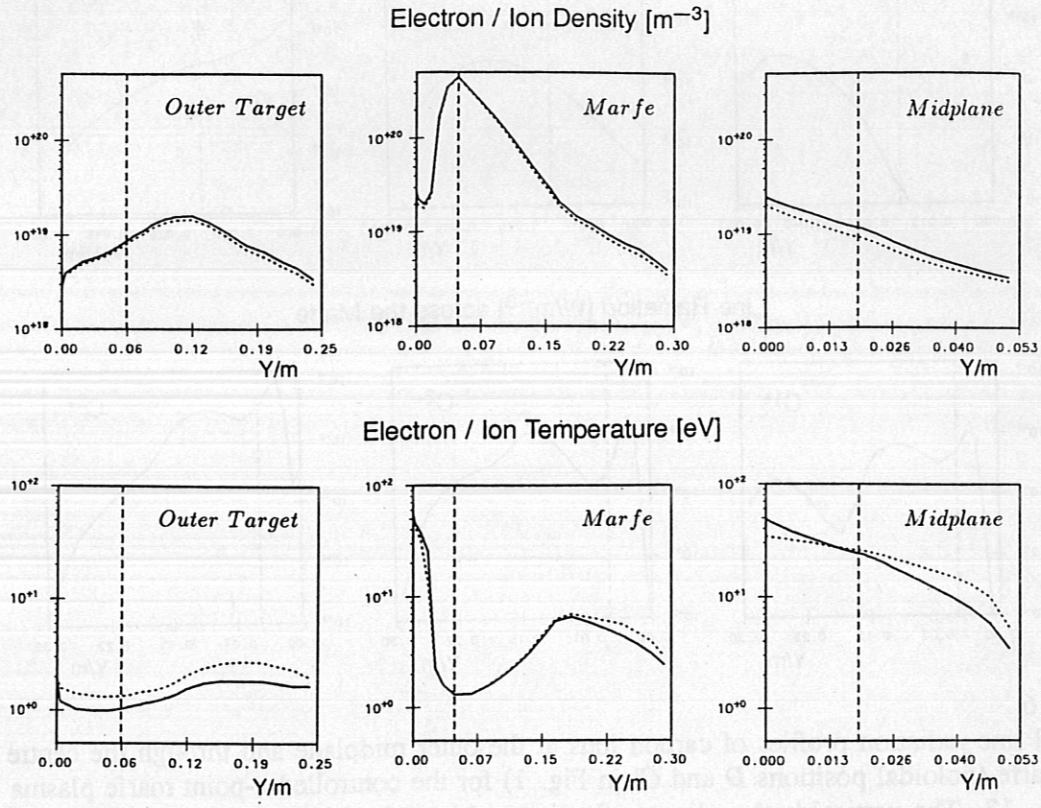

Fig. 17
Radial profiles of the electron density and temperature (full lines) and of the deuterium ion density and ion temperature (dotted lines) for the controlled plasma state of Fig. 13 (x-point marfe). The profiles are along the outer target plate, through the centre of the marfe and at the outer midplane (poloidal positions *B*, *C'* and *D* in Fig. 1).

First measurements of marfe radiation were made on ASDEX Upgrade with a CCD camera located at the level of the lower x-point and looking somewhat upward with respect to the horizontal. Figure 18a shows the picture of a marfe with double structure in the total light of the plasma obtained with this camera. Actually, the marfe consists of two toroidal belts at the high field side near the x-point. In order to compare these findings with code results, one may calculate the corresponding picture (as it would be seen by the camera) from the numerically obtained radiation field. An example is shown in Fig. 18b and Fig. 18c.

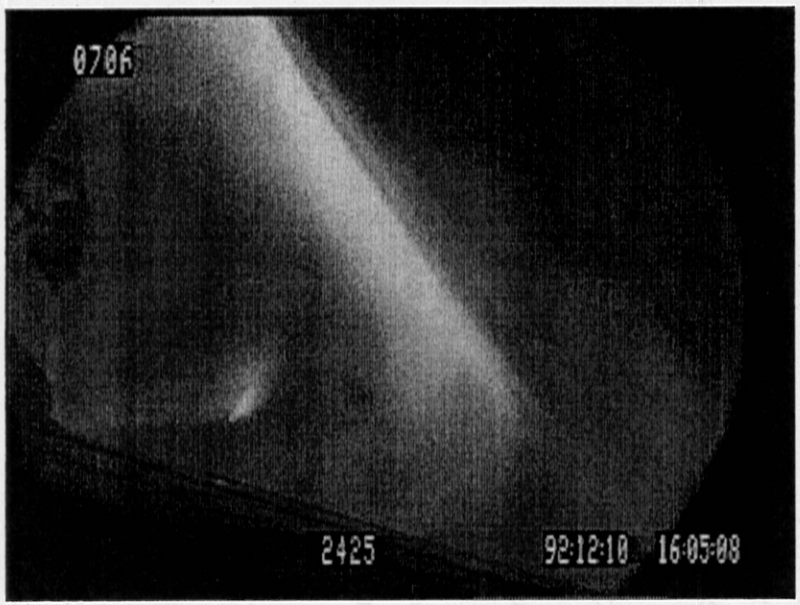

a)

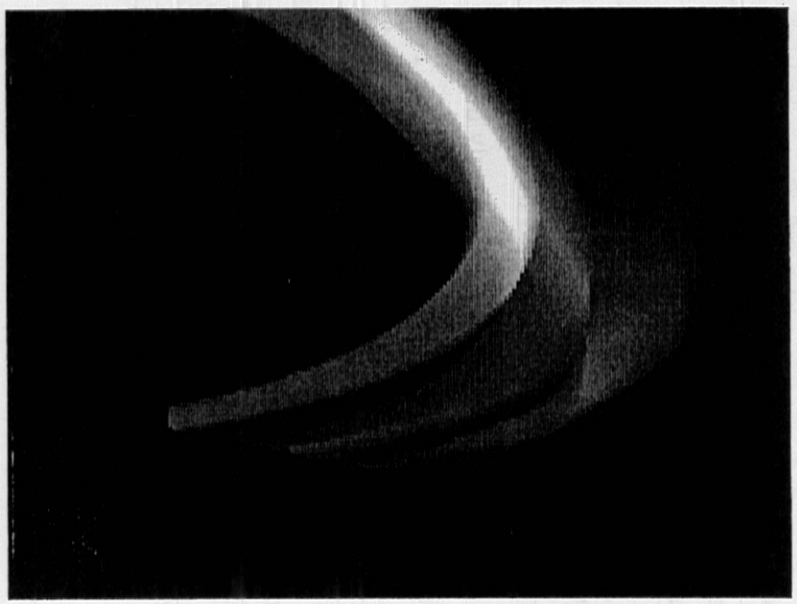

b)

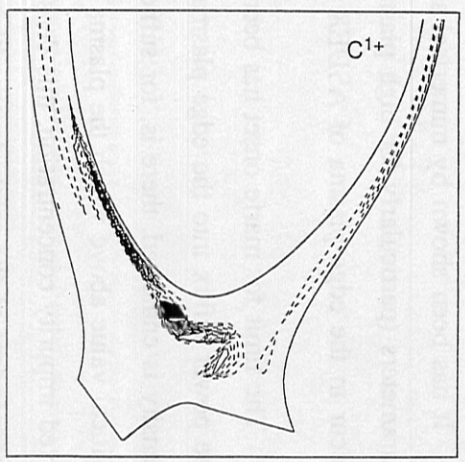

c)

Fig. 18
a) Photograph of a marfe with double structure taken with a CCD camera at ASDEX Upgrade
b) Picture of a marfe calculated from the radiation field in Fig. 18c
c) Marfe radiation field (C^{1+}) obtained from a multifluid calculation

6. Summary

It has been shown by numerical simulations that for certain ranges of the discharge parameters (particularly for high plasma density and impurity concentration) marfes will occur in the edge plasma of ASDEX Upgrade.

The limit for marfe onset has been determined as a function of the plasma density (n_e), the power influx into the edge plasma (P) and the safety factor (q). When the plasma density is enhanced, there is, for sufficiently high impurity concentration, a sharply defined critical value above which the plasma state abruptly reorganizes and a marfe is formed. For fixed impurity concentration, this density increases for increasing input power but is nearly independent of the safety factor although the relative density enhancement of the marfe (i.e. the growth rate) increases with q (the marfe becomes more pronounced for high q and flattens for decreasing q). The density limit shows a hysteresis which increases as the energy input and nearly vanishes below about 1 MW.

Time-dependent calculations with the full coupled multi-fluid code (deuterium, helium, carbon) show highly dynamic behaviour of marfes. Depending on the boundary conditions, marfes may move in a complicated way around the lower x-point and along the edge plasma (preferably at the inner side of the torus) or grow by their intrinsic dynamics and move to the bulk plasma. This behaviour is coupled to the motion of the lower impurity charge states, which provide effective radiative energy losses and thus cool the plasma. 'Steady-state' marfes which are well localized near the x-point can be sustained in a dynamic way by appropriately controlling the plasma density or impurity concentration.

Apart from extreme configurations, the density maximum (temperature minimum) of the marfe roughly coincides with the maximum of both the C^{2+} and C^{3+} line radiation. Although the radiation of both ion species should, therefore, be suitable for optical marfe diagnostics, the energy radiated by the marfe and the total energy radiated by the boundary plasma are clearly dominated by the C^{3+} line radiation.

It must be stressed that marfe formation as a highly nonlinear process depends crucially on the details of the model, and so at this stage the results are only of qualitative significance. Moreover, asymmetry effects with respect to the toroidal magnetic field direction which have been found experimentally / 13 / and the effect of carbon sources at the surfaces ('recycling') have not yet been taken into account. Further improvements of the model are,

therefore, in progress and will include in particular diamagnetic terms and a more consistent description of carbon 'recycling'.

References

/ 1 / G.B. Field, Astrophys. Journal 142 (1965) 531

/ 2 / J. Neuhauser, et al., Nucl. Fusion 26 (1986) 1679

/ 3 / J.F.Drake, Phys. Fluids 30 (1987) 2429

/ 4 / H. Capes, Ph. Ghendrih, A. Samain, Phys. Fluids B 4 (1992) 1287

/ 5 / J.A. Wesson, T.C. Hender, Nucl. Fusion 33 (1993) 1019

/ 6 / E.R. Müller, A. Stäbler, T. Hartinger et al., DRFC Report EUR-CEA-FC-1403, (Proc. of the Sat. Workshop of the 9th Int. Conf. on Plasma Surface Interactions), Cadarache 1990, p. 117

/ 7 / E.R. Müller, K.T. Hartinger et al., Proceedings of the 18th EPS Conf. on Controlled Fusion and Plasma Physics, Berlin 1991, p. I-117

/ 8 / A. Stäbler et al., Nucl. Fusion 32 (1992) 1557

/ 9 / A. Stäbler et al., Plasma Physics and Controlled Fusion Research 1992, Vienna, IAEA 1993, Vol. 2, p.523 (14th Conf. Proceedings, Würzburg 1992)

/ 10 / R. Schneider, D. Reiter et al., J. Nucl. Mater. 196-198 (1992) 810

/ 11 / McCormick et al., Proceedings of the 20th EPS Conf. on Controlled Fusion and Plasma Physics, Lisboa 1993, p. II-587

/ 12 / V. Mertens, K. Büchl, W. Junker et al., Proceedings of the 20th EPS Conf. on Controlled Fusion and Plasma Physics, Lisbon 1993, p. I-267

/ 13 / V. Mertens, W. Junker, M. Laux et al., to be published in "Plasma Physics and Controlled Fusion"

/ 14 / H. Kastelewicz, R. Schneider, J. Neuhauser et al., Contrib. Plasma Phys. 32 (1992) 456

/ 15 / H. Kastelewicz, R. Schneider, J. Neuhauser et al., Proceedings of the 20th EPS Conf. on Controlled Fusion and Plasma Physics, Lisbon 1993, p. II-807

/ 16 / M.F.A. Harrison, E.S. Hotston, G.P. Maddison, NET Report EUR-FU/XII-80/91/100., Febr. 1991